Available online at www.sciencedirect.com
ScienceDirect
Journal of Sound and Vibration 312 (2008) 606–629
JOURNAL OF SOUND AND VIBRATION
www.elsevier.com/locate/jsvi

Quantification of dynamic wheel–rail contact forces at short rail irregularities and application to measured rail welds

Michaël J.M.M. Steenbergen*

Railway Engineering Group, Faculty of Civil Engineering, Delft University of Technology, Stevinweg 1, NL 2628 CN Delft, The Netherlands

Received 9 January 2007; received in revised form 31 October 2007; accepted 5 November 2007
Available online 21 December 2007

Abstract

An analytical model for dynamic wheel–rail interaction at rail surface irregularities of arbitrary shape is presented. The model is formulated in the frequency domain and leads to relatively simple closed-form solutions for the variables which describe the dynamic interaction. With the help of the model, basic features of the dynamic wheel–rail interaction at short rail irregularities are identified. The focus is placed on short irregularities with a broad-band spectrum. The model is applied to calculate dynamic wheel–rail contact forces for a sample population of measured rail welds. General quantitative relationships between the rail geometry, the train speed and the level of the dynamic contact force are derived. Statistical distributions of geometrical properties of rail welds and the corresponding contact forces are derived. This allows for an easy estimation of the level of dynamic forces occurring over a railway network, given the availability of geometrical measurements.

1. Introduction

Continuously welded rail (CWR) nowadays is the standard in modern railway tracks, and the traditional bolted rail connections are often only still present in the form of insulated rail joints (IRJ) for detection and signalling purposes. The deflection of a bolted rail joint under a moving train axle loading leads to a high dynamic impact component, which is a source of rapid track deterioration and high noise levels, as pointed out in Refs. [1–3], and therefore the welded continuous connection was a significant improvement.

The most common types of rail welding are flash butt welding and aluminothermic or thermite welding. The application of the first type is almost fully automated, including the positioning of the rail ends to be joined, and therefore often applied in the construction of new tracks, whereas the second type requires handicraft and is therefore often applied in repair and maintenance work. However, the final grinding of the rail surface is in most cases done manually for both types of welding. Only in some cases the welds are being treated by a grinding train, on newly built tracks, yielding a high quality of the surface. In the literature, several studies have been published on rail welds, most of them dealing with metallurgical or related aspects. These aspects include the mechanical and micro-structural properties of welds [4], damage types occurring at welds [5],

*Tel.: +31 15 2783385; fax: +31 15 2783443.
E-mail address: M.J.M.M.Steenbergen@tudelft.nl

0022-460X/$ - see front matter © 2007 Elsevier Ltd. All rights reserved.
doi:10.1016/j.jsv.2007.11.004

testing and inspection methods [6], the effects of heat transfer during welding on defect formation [7,8], the effects of post-welding heat treatment [9], the measurement of residual stresses after welding [10,11] and their alleviation [12], fatigue crack growth in a weld under residual and temperature stresses [13] and the influence of loose sleepers on the bending fatigue of rail welds [14]. In Ref. [15] attention was paid to the relationship between train loading, weld geometry and weld failure modes. From measurements an approximately linear relationship was found between the train speed and the dynamic impact factor (DAF) occurring at welds.

Rail welds are very important in the context of dynamic wheel–rail interaction and track deterioration. In the majority of the cases, after welding a railhead irregularity along the rail results at the position of the weld. This can be due to inaccurate rail end positioning, the manual grinding of the rail surface, and in many cases the influence of inhomogeneous material shrinkage after cooling down in combination with early grinding. The irregularity has a typical length between 0.5 and 1 m. Therefore, in general the rail welds yield a significant contribution to the short-wave part of the track irregularity spectrum. This aspect the rail weld has in common with or other short track defects, such as short-pitch corrugations [16–18], squats [19,20], rail surface damage induced by rolling contact fatigue (RCF) [18,21–25], rail end unstraightness [26] and other geometrical imperfections of the wheel–rail interface. An overview is given in Ref. [27]. However, especially on new tracks the short-wave contribution is almost entirely determined by the rail weld geometry. This is very important due to its direct relation with the rate of track deterioration: the different frequency components of the power of the dynamic wheel–rail interaction force are dissipated in the vibrations of different components of the track–vehicle system, and consequently determine their rate of deterioration. Detection of short-wave track defects was addressed in, e.g. Refs. [28,29].

The relationship between the geometry of rail welds and the dynamic wheel–rail interaction has been dealt with extensively by Steenbergen and Esveld [30,31], on the basis of finite-element (FE) simulations for a number (239) of measured welds. However, these simulations have a number of disadvantages. These include the sensitivity of quantitative results in the high-frequency regime (500–2000 Hz) to filtering and damping (see also Refs. [32,33]), the validation of artificial damping and the simulation time needed for large measurement samples.

The investigation of the relationship between track geometry and interaction forces is relevant from another viewpoint. Railway track assessment is widely based on geometrical requirements without direct relationship to dynamic train–track interaction forces. This may be acceptable from the viewpoint of train passenger and vehicle ride comfort, but inconsistent from the viewpoint of track deterioration and the resulting necessity of maintenance, such as pointed out in, e.g. Ref. [34]. Therefore, in Refs. [30,31] also a more adequate assessment method for rail weld geometry was elaborated, relative to the conventional method which is based of the principle of vertical tolerances. The new method, which determines a Quality Index (QI) for the weld, dependent on the train speed for the track section, aims at a reduction of dynamic wheel–rail forces at welds and has been standardised in the Netherlands.

This paper investigates dynamic wheel–rail interaction at rail welds using an analytical approach. The method will be based on a simplified wheel–rail interaction model, and will be formulated in the frequency domain. The problems connected to FE modelling are avoided, but the method also has a disadvantage: because of the fact that the model is simplified and its linearity, it is not suitable for quantitative predictions with a high level of accuracy. The aim of the approach in this paper is therefore not to calculate quantitative results with a high level of accuracy, but to clarify the basic mechanisms in dynamic wheel–rail interaction due to short disturbances in the interface, to establish theoretical relationships, and to investigate trends. The results then can be compared to the FE results in Ref. [31]. Furthermore, the general formulations allow for an application of the results of the investigation on any wheel–rail interfacial irregularity with a broad-band spectrum.

The structure of this paper is as follows. In Section 2 a model for dynamic wheel–rail interaction is presented, together with the underlying assumptions. This model is described mathematically in Section 3, where also solutions for the main variables are derived. In Section 4 a model is presented to describe rail surface irregularities of arbitrary shape, representing the system excitation. Combination of the results of Sections 3 and 4 yields theoretical expressions for the wheel–rail contact force, which are analysed in Section 5. In Section 6, basic features of the dynamic wheel–rail interaction are discussed using model simulations for an elementary excitation. Simulation results for a set of measured rail welds are presented and discussed in

Section 7. These results are compared to the FE results obtained in Ref. [31]. Section 8 considers the dynamic wheel–rail interaction at rail welds on a railway network from a statistical viewpoint. In Section 9 the relation between the presence of rail welds and the occurrence of corrugation is discussed, and conclusions are presented.

2. Model for dynamic wheel–rail interaction at short rail irregularities

The following assumptions are adopted in the model being used to analyse the dynamic wheel–rail contact:

1. The irregularity of the rail surface is short compared to the ratio of the train speed to the eigenfrequency of the bogie motion. Under these circumstances ($f > 20$ Hz), the wheelset motion may be considered as isolated from the bogie and car body motion. Generally, this holds for welding irregularities, which have a length-scale of about 1 m [30]. In this case, only the unsprung vehicle mass of the vehicle plays a role.
2. Wave propagation in the rail as well as physical damping mechanisms are not accounted for. The energy input in the rail due to the dynamic contact force generated by the rail irregularity is mostly radiated into the rail at the contact point and dissipated in the rail system components, mainly the railpads and the ballast. However, in order to determine the local maximum dynamic wheel–rail contact force which occurs at some point along an irregularity, a relatively short time-scale is considered. Wave propagation and damping mechanisms are irrelevant within these small time-scales; they only play a role at increasing time scales.
3. The considered irregularities lead to continuous single-point contact in time. Transient double-point contact between wheel and rail leads to completely different mechanisms in the wheel–rail interaction, as has been shown in Ref. [1], and is therefore avoided. This is realistic for rail welds (but not for rail joints, like IRJ or bolted connections).
4. The rail is modelled as continuously supported. This is a significant simplification, which will especially affect the model results for welding irregularities having a predominant wavelength that is comparable to the sleeper spacing distance. However, this simplification is justified by the following reasons. As has been mentioned in the Introduction, it is not the primary aim of this paper to predict quantitative results with a high level of accuracy, but to investigate basic features that can explain trends. Moreover, rail welding irregularities generally have a broad-band spectrum and do not exhibit any preferred wavelength. Therefore, the broad spectrum of the excitation has an averaging effect on peaks in the track receptance. This effect becomes even stronger when trends are considered for a large number of measured welds. Finally, it was shown in Ref. [31] that the shortest waves in the rail irregularity generate the highest peak contact forces. This is because the inertia of the system dominates the response. Since these peak forces are mainly of interest in this study, the rail support is less relevant. For a comparison of receptance functions of continuously and discretely supported rails, and the effect of the sleeper positions, see e.g. Refs. [32,35–37].

In Fig. 1 two models are shown for dynamic wheel–rail interaction analysis at short rail irregularities with a broad-band spectrum; some notations are introduced in the figures. In the model in Fig. 1a the unsprung mass

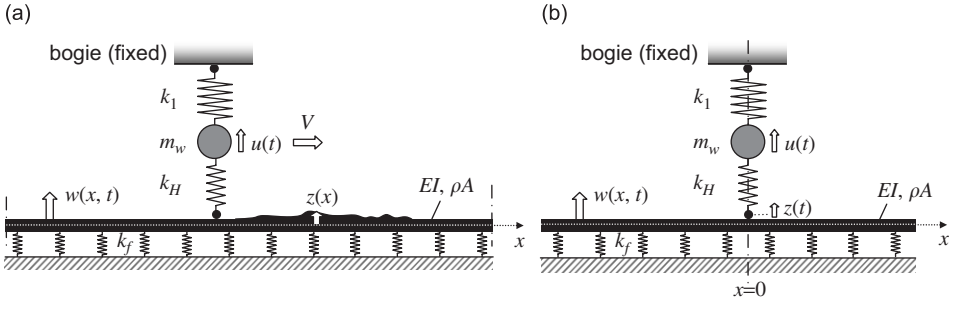

Fig. 1. Wheel–rail interaction models; moving wheel model on geometrical rail irregularity $z(x)$ (a) and equivalent standing wheel model with excitation $z(t)$ (b).

of a train axle moves with a speed V along the rail. With respect to the vehicle, the unsprung mass of an axle, the Hertzian contact stiffness and the primary suspension stiffness are included in the model. The vertical geometry of the rail, which is continuously supported, is described by $z(x)$. This moving wheel problem may be simplified to a standing wheel problem, based on assumption (2). This approach is widely accepted in the investigation of dynamic wheel–rail interaction in the high-frequency regime (see e.g. Refs. [36,38]). The standing wheel model is shown in Fig. 1b. The excitation—as the Hertzian spring contact rolls over the rail geometry $z(x)$ at velocity V—changes into an excitation $z(t)$ of the Hertzian contact spring at $x = 0$ as a function of time.

3. Mathematical problem formulation and solution

The mathematical statement for the model as shown in Fig. 1b is given in the following. The equation of motion for the rail is given by

$$EI\frac{\partial^4 w(x,t)}{\partial x^4} + \rho A\frac{\partial^2 w(x,t)}{\partial t^2} + k_f w(x,t) = -F(t)\delta(x). \tag{1}$$

The equation of motion for the wheel system is given by

$$m_w\frac{\mathrm{d}^2 u(t)}{\mathrm{d}t^2} + k_1 u(t) = F(t). \tag{2}$$

The contact force in the wheel–rail contact point is given as

$$F(t) = k_H(-u(t) + w(0,t) + z(t)). \tag{3}$$

Assuming an infinitely small but non-zero damping in the system, the rail is undisturbed at $x = \pm\infty$ at any time moment (i.e., Sommerfeld's radiation conditions must be satisfied). Further, all initial conditions are assumed zero:

$$u(0) = \dot{u}(0) = 0 \ \text{ and } \ w(x,0) = \dot{w}(x,0) = 0. \tag{4}$$

Since the model is linear, the static load and the resulting steady-state rail displacement field are not taken into consideration; only the dynamic contact force and dynamic beam deflections are considered. Further, a linearised Hertzian spring is adopted in the model in order to enable an analytical approach in the frequency domain; this assumption and its validity domain will be discussed in Section 6. The equation of motion (1) of the beam in the t, x domain is rewritten as

$$\frac{\partial^4 w(x,t)}{\partial x^4} + \frac{1}{a^2}\frac{\partial^2 w(x,t)}{\partial t^2} + b^2 w(x,t) = -\frac{1}{EI}F(t)\delta(x) \ \text{ with } \ a = \sqrt{\frac{EI}{\rho A}}, \quad b = \sqrt{\frac{k_f}{EI}}. \tag{5}$$

Laplace-transforming this equation with respect to time, with $w(x,0) = \dot{w}(x,0) = 0$, yields

$$\frac{\tilde{\partial}^4 \tilde{w}(x,s)}{\partial x^4} + \left(\frac{s^2}{a^2} + b^2\right)\tilde{w}(x,s) = -\frac{1}{EI}\tilde{F}(s)\delta(x) \tag{6}$$

with the transformed variable indicated by a tilde. Because the beam is undisturbed at $x = \pm\infty$ for any time moment, the solution for the governing variable will be determined by applying a Fourier transformation with respect to x to Eq. (6). The applied Fourier transform is defined according to

$$\bar{\alpha}(k_x) = \int_{-\infty}^{\infty} \alpha(x)\,\mathrm{e}^{\mathrm{i}k_x x}\,\mathrm{d}x. \tag{7}$$

The Fourier transformed governing equation (6) is given by

$$\bar{\tilde{w}}(k,s)(k^4 + s^2/a^2 + b^2) = -\frac{1}{EI}\tilde{F}(s) \tag{8}$$

with the forward Fourier-transformed variable indicated by a bar. This yields for the solution $\bar{\tilde{w}}$:

$$\bar{\tilde{w}}(k,s) = -\frac{1}{EI}\frac{\tilde{F}(s)}{k^4 + s^2/a^2 + b^2}. \tag{9}$$

The inverse Fourier transform of this solution yields the following particular solution in the x,s domain:

$$\tilde{w}(x,s) = -\frac{\tilde{F}(s)}{2\pi EI}\int_{-\infty}^{\infty}\frac{\mathrm{e}^{-\mathrm{i}kx}}{k^4 + s^2/a^2 + b^2}\,\mathrm{d}k. \tag{10}$$

The integral can be calculated by contour integration, adding a semicircle joining $-\infty$ to ∞ and applying, respectively, Jordan's lemma and Cauchy's residue theorem. The poles of the integrand are equal to the solutions of the equation

$$k^4 + s^2/a^2 + b^2 = 0 \Rightarrow k_{1,2,3,4} = (\pm 1 \pm \mathrm{i})k_0, \quad k_0 = \frac{1}{\sqrt{2}}\sqrt[4]{\frac{s^2}{a^2} + b^2}. \tag{11}$$

The individual poles are written as

$$k_1 = (1+\mathrm{i})k_0, \quad k_2 = (-1+\mathrm{i})k_0, \quad k_3 = (-1-\mathrm{i})k_0, \quad k_4 = (1-\mathrm{i})k_0. \tag{12}$$

By analysis of the roots it can be shown that for all $\sigma > 0$ ($s = \sigma + \mathrm{i}\omega$), a and b, independently of the sign of ω, holds: $\mathrm{Im}(k_1) > 0$, $\mathrm{Im}(k_2) > 0$, $\mathrm{Im}(k_3) < 0$, $\mathrm{Im}(k_4) < 0$. Or, poles k_1 and k_2 are situated in the upper half-plane and k_3 and k_4 in the lower half-plane of the complex k-plane.

According to Jordan's lemma, $\lim_{R\to\infty}\int_C f(k)\,\mathrm{e}^{-\mathrm{i}kx}\,\mathrm{d}x = 0$ $(x > 0)$ if the closing contour C is in the third and fourth quadrant (lower half-plane), and $f(k)$ tends uniformly to zero for increasing radius R of the contour. An analogous statement holds for $x < 0$, yielding a closing contour in the upper half-plane of the complex k-plane. Since the integrand is single-valued, Cauchy's residue theorem can be applied now. First it will be applied for the first contour, $x > 0$; 2 poles are situated inside the contour. The residue theorem states

$$\int_{-\infty}^{\infty}\frac{\mathrm{e}^{-\mathrm{i}kx}}{k^4 + s^2/a^2 + b^2}\,\mathrm{d}k = 2\pi\mathrm{i}\sum_{k_1,k_2}\text{Residue of }\frac{\mathrm{e}^{-\mathrm{i}kx}}{k^4 + s^2/a^2 + b^2}\text{ at } k_{1,2} = 2\pi\mathrm{i}\sum_{k_1,k_2}\left.\frac{\mathrm{e}^{-\mathrm{i}kx}}{4k^3}\right|_{k_{1,2}}. \tag{13}$$

Evaluating this expression with the poles defined by Eq. (12) yields

$$\begin{aligned}\int_{-\infty}^{\infty}\frac{\mathrm{e}^{-\mathrm{i}kx}}{k^4 + s^2/a^2 + b^2}\,\mathrm{d}k &= 2\pi\mathrm{i}\sum_{k_1,k_2}\left.\frac{\mathrm{e}^{-\mathrm{i}kx}}{4k^3}\right|_{k_{1,2}} = 2\pi\mathrm{i}\left(\frac{\mathrm{e}^{-\mathrm{i}(1+\mathrm{i})k_0x}}{4((1+\mathrm{i})k_0)^3} + \frac{\mathrm{e}^{-\mathrm{i}(-1+\mathrm{i})k_0x}}{4((-1+\mathrm{i})k_0)^3}\right)\\ &= \frac{\pi}{8k_0^3}\left((1-\mathrm{i})\,\mathrm{e}^{(1-\mathrm{i})k_0x} + (1+\mathrm{i})\,\mathrm{e}^{(1+\mathrm{i})k_0x}\right).\end{aligned} \tag{14}$$

Similarly, the expression for the second closed contour can be found (the contour is in the negative sense; a minus should be added), lower half-plane, $x > 0$:

$$\begin{aligned}\int_{-\infty}^{\infty}\frac{\mathrm{e}^{-\mathrm{i}kx}}{k^4 + s^2/a^2 + b^2}\,\mathrm{d}k &= -2\pi\mathrm{i}\sum_{k_3,k_4}\left.\frac{\mathrm{e}^{-\mathrm{i}kx}}{4k^3}\right|_{k_{3,4}} = -2\pi\mathrm{i}\left(\frac{\mathrm{e}^{-\mathrm{i}(-1-\mathrm{i})k_0x}}{4((-1-\mathrm{i})k_0)^3} + \frac{\mathrm{e}^{-\mathrm{i}(1-\mathrm{i})k_0x}}{4((1-\mathrm{i})k_0)^3}\right)\\ &= \frac{\pi}{8k_0^3}\left((1-\mathrm{i})\mathrm{e}^{(-1+\mathrm{i})k_0x} + (1+\mathrm{i})\mathrm{e}^{(-1-\mathrm{i})k_0x}\right).\end{aligned} \tag{15}$$

If $x < 0$ then $x = -|x|$, whereas if $x > 0$ then $x = |x|$. Therefore, the integral can be evaluated for arbitrary x as

$$\int_{-\infty}^{\infty}\frac{\mathrm{e}^{-\mathrm{i}kx}}{k^4 + s^2/a^2 + b^2}\,\mathrm{d}k = \frac{\pi}{8k_0^3}\left((1-\mathrm{i})\,\mathrm{e}^{(-1+\mathrm{i})k_0|x|} + (1+\mathrm{i})\,\mathrm{e}^{(-1-\mathrm{i})k_0|x|}\right). \tag{16}$$

Substituting Eq. (16) into Eq. (10) yields the solution in the x,s domain for the load. This solution is given by

$$\tilde{w}(x,s) = -\frac{\tilde{F}(s)}{16EIk_0^3}\left((1-\mathrm{i})\,\mathrm{e}^{(-1+\mathrm{i})k_0|x|} + (1+\mathrm{i})\,\mathrm{e}^{(-1-\mathrm{i})k_0|x|}\right), \quad k_0 = \frac{1}{\sqrt{2}}\sqrt[4]{\frac{s^2}{a^2}+b^2}. \tag{17}$$

Next, expressions are derived for the oscillator, i.e. the wheel mass. Assuming $u(0) = \dot{u}(0) = 0$, its equation of motion, Laplace-transformed with respect to time (the transformed variable is indicated by a tilde), is given as follows:

$$\left(m_w s^2 + k_1\right)\tilde{u}(s) = \tilde{F}(s) \Rightarrow \tilde{u}(s) = \frac{\tilde{F}(s)}{m_w s^2 + k_1}. \tag{18}$$

The coupling between Eqs. (17) and (18) is established through the interaction force according to Eq. (3). The Laplace-transform of this expression is given by

$$\tilde{F}(s) = k_H(-\tilde{u}(s) + \tilde{w}(0,s) + \tilde{z}(s)). \tag{19}$$

Substitution of expressions (17) for $\tilde{w}(0,s)$ and (18) for $\tilde{u}(s)$ yields, after some elaboration, the final expression for the contact force $\tilde{F}(s)$ in the Laplace-domain is given as (with $s = \sigma + \mathrm{i}\omega$):

$$\tilde{F}(s) = \frac{\tilde{z}(s)}{1/k_H + 1/(m_w s^2 + k_1) + 1/\left(8EIk_0^3\right)} \text{ with } k_0 = \frac{1}{\sqrt{2}}\sqrt[4]{\frac{1}{EI}(\rho A s^2 + k_f)}. \tag{20}$$

The wheel displacement is given by Eq. (18). Substitution of Eq. (20) yields

$$\tilde{u}(s) = \frac{\tilde{z}(s)}{1 + (m_w s^2 + k_1)\left(1/k_H + 1/\left(8EIk_0^3\right)\right)}. \tag{21}$$

An explicit expression for the rail displacement at the contact point can be found by substituting Eqs. (18) and (20) into Eq. (19):

$$\tilde{w}(0,s) = \tilde{z}(s)\left(2 - \frac{1}{8EIk_0^3\left(1/k_H + 1/(m_w s^2 + k_1)\right) + 1}\right). \tag{22}$$

The expressions (20)–(22) must be transformed to the time domain. This inverse Laplace-transform (which is basically an integration over the frequency) will be computed numerically. Because of the fact that the integrand is not single-valued (due to the presence of radicals), the analytical inverse transform, by means of contour integration, implies the more complex branch cutting. The numerical procedure is explained in the following. The inverse Laplace-transform of $\tilde{F}(s)$ is defined as

$$F(t) = \frac{1}{2\pi\mathrm{i}}\int_{\sigma-\mathrm{i}\infty}^{\sigma+\mathrm{i}\infty} \tilde{F}(s)\,\mathrm{e}^{st}\,\mathrm{d}s. \tag{23}$$

Substituting $s = \sigma + \mathrm{i}\omega$ with σ some small positive real value, or $\mathrm{d}s = \mathrm{i}\,\mathrm{d}\omega$, and $-\infty < \omega < \infty$, yields:

$$F(t) = \frac{\mathrm{e}^{\sigma t}}{2\pi}\int_{-\infty}^{\infty} \tilde{F}(\sigma + \mathrm{i}\omega)\,\mathrm{e}^{\mathrm{i}\omega t}\,\mathrm{d}\omega. \tag{24}$$

The integrand in this expression can be elaborated as follows:

$$\begin{aligned}\tilde{F}\,\mathrm{e}^{\mathrm{i}\omega t} &= \left(\mathrm{Re}(\tilde{F}) + \mathrm{i}\,\mathrm{Im}(\tilde{F})\right)(\cos\,\omega t + \mathrm{i}\,\sin\,\omega t)\\ &= \underbrace{\mathrm{Re}(\tilde{F})\cos\,\omega t - \mathrm{Im}(\tilde{F})\sin\,\omega t}_{\text{Real part}} + \mathrm{i}\,\underbrace{\left(\mathrm{Re}(\tilde{F})\sin\,\omega t + \mathrm{Im}(\tilde{F})\cos\,\omega t\right)}_{\text{Imaginary part}},\end{aligned} \tag{25}$$

where the imaginary part of the integrand should add up to 0, as the force $F(t)$ is real. This means, $\sin\omega t$ being anti-symmetric and $\cos\omega t$ symmetric with respect to ω, that $\mathrm{Re}(\tilde{F})$ is a symmetric and $\mathrm{Im}(\tilde{F})$ an

anti-symmetric function of ω. Therefore, the integral (24) may be written as follows:

$$F(t) = \frac{e^{\sigma t}}{2\pi}\int_{-\infty}^{\infty} \mathrm{Re}\left(\tilde{F}(s)\,e^{i\omega t}\right) d\omega = \frac{e^{\sigma t}}{\pi}\int_{0}^{\infty} \mathrm{Re}\left(\tilde{F}(s)\,e^{i\omega t}\right) d\omega. \tag{26}$$

This last expression will be used for numerical integration of solutions (20)–(22) in the Laplace domain.

In summary, the general expressions (in integral form) for the dynamic wheel–rail contact force, the wheel displacement and the rail displacement in the contact point are given as a function of time, for an excitation function $z(t)$ with Laplace-image $\tilde{z}(s)$, by

$$F(t) = \frac{e^{\sigma t}}{\pi}\int_{0}^{\infty} \mathrm{Re}\left(\frac{\tilde{z}(s)}{1/k_H + 1/(m_w s^2 + k_1) + 1/\left(8EIk_0^3\right)}\,e^{i\omega t}\right) d\omega, \tag{27}$$

$$u(t) = \frac{e^{\sigma t}}{\pi}\int_{0}^{\infty} \mathrm{Re}\left(\frac{\tilde{z}(s)}{1 + (m_w s^2 + k_1)\left(1/k_H + 1/\left(8EIk_0^3\right)\right)}\,e^{i\omega t}\right) d\omega, \tag{28}$$

$$w(0,t) = \frac{e^{\sigma t}}{\pi}\int_{0}^{\infty} \mathrm{Re}\left(\tilde{z}(s)\left(2 - \frac{1}{8EIk_0^3\left(1/k_H + 1/(m_w s^2 + k_1)\right) + 1}\right)e^{i\omega t}\right) d\omega$$

$$\text{with}\quad k_0 = \frac{1}{\sqrt{2}}\sqrt[4]{\frac{1}{EI}\left(\rho A s^2 + k_f\right)}, \quad s = \sigma + i\omega. \tag{29}$$

4. Elementary model for description of rail surface irregularities

As has been stated in the Introduction, the present study focuses mainly on rail welds as a field of application. In Refs. [30,31] a model for the vertical geometry of rail welds was proposed and developed; the aim was to describe real measurements, and therefore the model was discrete. According to Ref. [30], the surface of a rail weld may be described in the longitudinal direction by a sequence of discrete slopes which are Gaussian distributed with zero mean value. Such a spatial or temporal sequence of slopes can be represented as a summation of terms in the Laplace-domain, due to the linearity of this transform. This property will allow for a simple derivation of some basic relationships for arbitrary irregularities. The vertical rail surface is described as a function of the longitudinal coordinate x ($x \geqslant 0$) by

$$\begin{aligned} z(x) = {} & \theta_1 x H(\Delta x - x) + ((\theta_1 - \theta_2)\Delta x + \theta_2 x)H(x - \Delta x)H(2\Delta x - x) \\ & + ((\theta_1 + \theta_2 - 2\theta_3)\Delta x + \theta_3 x)H(x - 2\Delta x)H(3\Delta x - x) \\ & + \cdots + (\theta_1 + \theta_2 + \theta_3 + \cdots)\Delta x H(x - 3\Delta x). \end{aligned} \tag{30}$$

The model is shown in Fig. 2a for the elementary case of a ramp with a single slope, and in Fig. 2b for an irregularity comprising more discrete slopes.

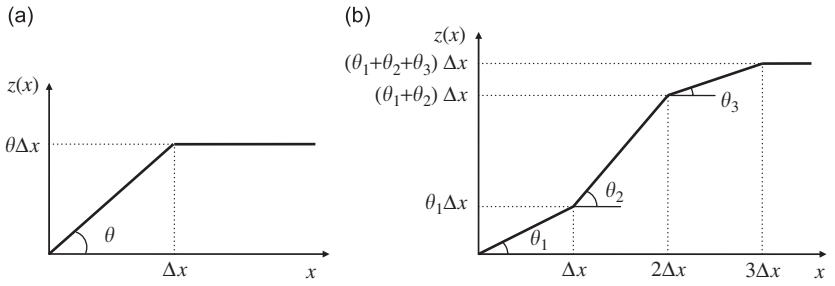

Fig. 2. Quasi-discrete models to describe longitudinal wheel–rail contact surface irregularities; basic model with linear irregularity (ramp) (a) and multi-linear irregularity (b).

The expression in the time-domain becomes

$$z(t) = \theta_1 VtH(\Delta x/V - t) + ((\theta_1 - \theta_2)\Delta x + \theta_2 Vt)H(t - \Delta x/V)H(2\Delta x/V - t) + ((\theta_1 + \theta_2 - 2\theta_3)\Delta x + \theta_3 Vt)H(t - 2\Delta x/V)H(3\Delta x/V - t) + \cdots + (\theta_1 + \theta_2 + \theta_3 + \cdots)\Delta x H(t - 3\Delta x/V). \quad (31)$$

The Laplace-image of a sequence of N discrete slopes becomes

$$\tilde{z}(s) = \frac{V}{s^2}\left(1 - \mathrm{e}^{-s\Delta x/V}\right)\sum_{n=1}^{N}\theta_n \mathrm{e}^{-(n-1)s\Delta x/V}, \quad 1 \leqslant n \leqslant N. \quad (32)$$

5. Parametrical analysis of the wheel–rail contact force

Substitution of Eq. (32) into Eq. (27) for the contact force yields an explicit integral expression for this force. For a single ramp (with a single discrete slope, as depicted in Fig. 2a) the expression becomes

$$F_{\mathrm{contact}}(t) = \frac{\theta V}{\pi}\int_0^{\infty} \mathrm{Re}\left(\frac{\left(1 - \mathrm{e}^{-s\Delta x/V}\right)/s^2}{1/k_H + 1/(m_w s^2 + k_1) + 1/\left(8EIk_0^3\right)}\mathrm{e}^{\sigma t}\,\mathrm{e}^{\mathrm{i}\omega t}\right)\mathrm{d}\omega. \quad (33)$$

For the sequence of N discrete slopes, the expression for the contact force may be written as follows:

$$F(t) = \frac{1}{\pi}V\sum_{n=1}^{N}\theta_n\int_0^{\infty}\mathrm{Re}(f_n(s))\,\mathrm{d}\omega \quad (34)$$

in which

$$s = \sigma + \mathrm{i}\omega, \quad f_n(s) = \frac{\left(1 - \mathrm{e}^{-s\Delta x/V}\right)\mathrm{e}^{-(n-1)s\Delta x/V}}{1/k_H + 1/(m_w s^2 + k_1) + 1/\left(8EIk_0^3\right)}\frac{\mathrm{e}^{st}}{s^2}. \quad (35)$$

It follows from Eq. (33) that a theoretical perfectly linear relationship exists between the slope of a ramp and the dynamic contact force in the time domain. The relation between the contact force and the velocity cannot be extracted explicitly from Eq. (33), but it will be shown later on that also this relationship is perfectly linear. The same can be observed for the rail and wheel displacements in the time domain, according to Eqs. (28) and (29).

It is noted that the time history of expression (34) consists of a linear superposition of terms (33) giving the force occurring for a single ramp (as is expected for a linear system). This means that the component of the force for each discrete slope θ_n as a function of time is proportional to θ_n. However, the maximum of Eq. (34) is only reached for $\theta_{\max}$ if the time functions (the results of the integration over the frequency) in the separate terms do not interact. This is not necessarily the case, and for an arbitrary geometry a mutual influence must be expected, especially as the sampling basis Δx approaches zero. Therefore, a perfectly linear relation between

Table 1
Model parameter values

Parameter	Value
Static wheelload, Q	112.5×10^3 N
Wheel radius, R_{wheel}	0.46 m
Transversal railhead radius, R_{railhead}	0.3 m
Wheel mass (half unsprung mass), m_w	900 kg (ICM-III passenger train)
Primary suspension stiffness, k_1	2×10^6 N/m
Rail bending stiffness, EI	4.25×10^6 N m^2 (54 E1)
Rail distributed mass, ρA	54.4 kg/m (54 E1)
Rail support stiffness, k_f	50×10^6 N/m^2

$F_{\max}$ and $\theta_{\max}$ does not exist. The bandwidth of such a relationship depends on the statistical distribution of the slopes for a considered discretely sampled weld population (or alternatively, the wavelength-spectrum of a weld population). This subject will be discussed in Sections 7 and 8.

6. Basic features of the dynamic wheel–rail interaction

In. Eq. (18) a linearisation of the nonlinear Hertzian contact stiffness has been applied to enable an approach in the frequency domain. The linearisation is applied at the level of the static wheelload (which is chosen as 112.5 kN), yielding a tangent stiffness. Application of the geometrical parameters according to Table 1 then results into the following expression (according to Ref. [39]):

$$k_H = \sqrt[3]{8\times10^{22}Q\sqrt{R_{\text{wheel}}R_{\text{railhead}}}} = \sqrt[3]{3\times10^{22}Q}. \tag{36}$$

The resulting linear stiffness will lead to reliable results for dynamic load fluctuations around this level. According to the simplified expression (36), the Hertzian stiffness is governed by the third root of the wheelload. Therefore, model results may be considered as reliable when the dynamic amplification factor (DAF) does not exceed 2, as is clear from the following relationship:

$$k_H(2Q) = \sqrt[3]{2}k_H(Q) \approx 1.26k_H(Q). \tag{37}$$

The smaller the value for the DAF, the higher the accuracy of the contact force will be. As will be shown later on, in the region of interest of the irregularities to be considered, the DAF does not exceed a factor 2. Unless indicated differently, the simulations in this and following sections use the parameter values indicated in Table 1. Representative values have been chosen for the involved parameters. The static wheelload corresponds to the nominal axle load of 225 kN which is allowed in many countries for conventional rail traffic [39]. The rail properties of the standard 54 E1 profile are used. The value for the rail support stiffness is the one which is used in the design of embedded rail structures [40]. The adopted wheel mass corresponds to an unsprung mass of 1800 kg, which is a common value for conventional passenger trains. No damping is present. This is expected to have a negligible influence on the first impact force in the contact, as it is dominated by the wheel and rail inertia, and the damping in the wheel–rail interface is negligible.

The studied wheel–rail system can be characterised in the frequency-domain by means of the spectrum $\tilde{F}(\omega)$ of the contact force due to a unit pulse excitation $\tilde{z}(s) = 1$ (according to Eq. (20); $s = \sigma + \mathrm{i}\omega$ with $\sigma = 0$). The absolute value of this spectrum is shown in Fig. 3. A narrow and sharp peak appears around 45 Hz, followed by a gradually increasing and declining frequency content in the region between 200 and 3000 Hz, with a maximum around 1000 Hz. The peak at the lower frequency is completely governed by the rail support

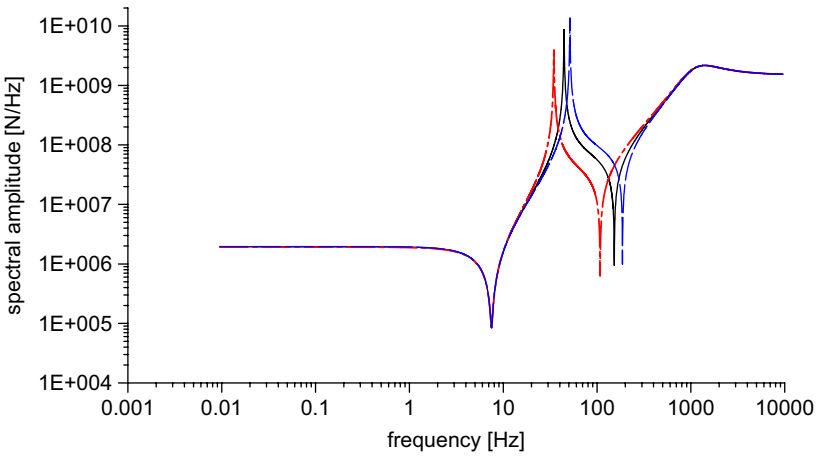

Fig. 3. Absolute value of the spectrum of the contact force in the wheel–rail system due to a unit pulse excitation: reference (——); support stiffness increased with 50% (— – —); and support stiffness reduced with 50% (— —).

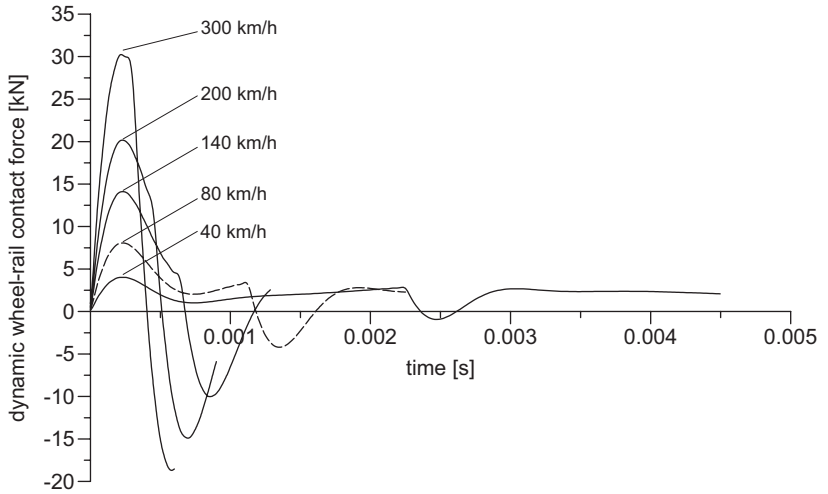

Fig. 4. Time histories of the wheel–rail contact force for a ramp with an inclination of 2 mrad, a basis of 25 mm and different train velocities.

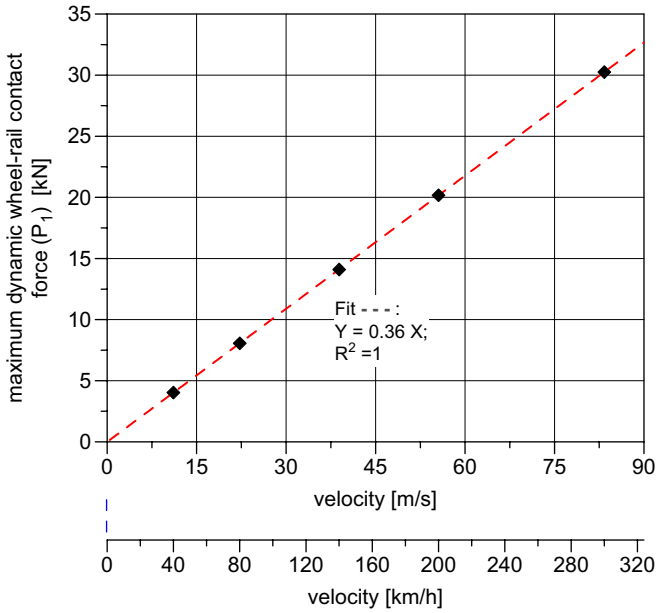

Fig. 5. Relationship between the maximum dynamic contact force (P_1) and the velocity, for a given ramp inclination (2 mrad) and basis length (25 mm).

stiffness, as is shown in Fig. 3 for two variations of this stiffness. In the integration process for the excitations that will be considered, this peak only has a minor contribution, indicating a limited impact of the support stiffness on the time-domain response.

In the following, the influence of the velocity in Eq. (34) is considered, for the basic case of a single ramp. Because the linear influence of the slope θ is known, θ is kept constant at 2 mrad. The contact force is then calculated for the velocities $v = 11.1$, 22.2, 38.9, 55.6 and 83.3 m/s (which is 40, 80, 140, 200 and 300 km/h). For each case the maximum value of the contact force is determined, occurring in the time interval $2\Delta x/V$. The length of the basis is chosen as $\Delta x = 25$ mm. The time histories of these contact forces are shown in Fig. 4 for a duration $2\Delta x/V$. The contact force increases with the velocity, and for lower velocities a dip in the contact force occurs after reaching the transition from the inclined part of the ramp to the horizontal part.

The extreme values of the force using a basis of 5 mm show no consistent trend, because for high velocities the time interval corresponding to this length is too short for the force to reach its first peak that would occur without the second transition in the ramp, from the inclined part of the ramp to the horizontal part (apart from the fact that a real contact patch is larger than 5 mm). For a basis of 25 mm this is no longer the case; the trend of the maximum dynamic contact force as a function of the velocity is shown in Fig. 5. It can be concluded that for a rail irregularity with a single constant slope, the first peak force (commonly denoted as P_1) is perfectly and directly proportional to the speed.

In Ref. [31], the following approximate relationship has been established between the maximum dynamic force occurring at rail welds, their maximum absolute inclination, and the train speed:

$$F_{\mathrm{dyn,\,max}} = \gamma\, V\, \theta \;\; (\text{with } \theta = \tan\theta) \quad (F\,(kN), \quad V\,(\mathrm{m/s}), \quad \theta\,(\mathrm{mrad})). \tag{38}$$

In Ref. [31] the factor $\gamma = 0.22$ was found for this relationship. According to Fig. 5 the following relationship is found for a ramp with a single slope:

$$F_{\mathrm{dyn,\,max}} = 0.36\, V \;\; \text{for} \;\; \theta = 2\,\mathrm{mrad}, \;\; \text{or} \;\; \gamma = 0.18. \tag{39}$$

The coefficients found in both cases are very similar. It is noted that the dimensions in Eqs. (38) and (39) are inconsistent for a dimensionless coefficient γ, which is non-physical. It is therefore useful to return to the original expression (33) for the contact force; the dimensions in this equation are as follows:

$$F\,[\mathrm{kN}] = \theta\,[\mathrm{mrad}]\, V\,[\mathrm{ms^{-1}}] \quad \int_0^{\infty} \mathrm{Re}\left(\frac{K}{s^2}\right)\left[\frac{\mathrm{Nm^{-1}}}{\mathrm{s^{-2}}}\right] \mathrm{d}\omega\,[\mathrm{s^{-1}}]. \tag{40}$$

In Eq. (40) K represents some overall stiffness parameter. Comparing Eqs. (38) and (39) to Eq. (40) it is obvious that the integral expression has been replaced by the constant γ, which therefore should have a dimension (namely (N s/m)), accounting for the effect of a dynamic system stiffness (in which all masses and stiffnesses in the system are involved). Eqs. (38) and (39) can be used alternatively in a normalised form, with a dimensionless coefficient.

In Fig. 6 the effect of the length of the basis on the wheel–rail interaction is shown, for $\theta = 2$ mrad, $V = 38.9$ m/s (140 km/h). The P_1 force needs a basis of about 10 mm (which is approximately the size of the contact patch) in order to reach its 'natural' peak value. If the basis is long enough, a narrow and a broad peak appear in the contact force (the P_1 and P_2 force, respectively). For the considered parameters (and without damping), the magnitude of P_2 exceeds P_1.

The effect of different track parameters on the P_1 and P_2 forces is shown in Fig. 7. Simulations have been performed for a doubled and a halved foundation stiffness with respect to the reference situation, and a rail bending stiffness and a rail inertia both reduced with a factor 5. From this figure it can be concluded that the rail inertia, and to a lesser degree, the rail bending stiffness, govern the P_1 force, whereas the rail support stiffness, and to a small extent the rail bending stiffness, govern the P_2 force.

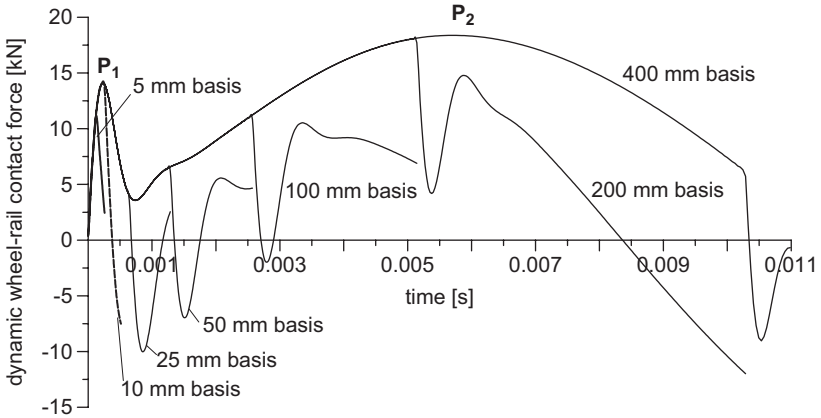

Fig. 6. Influence of the basis length of the ramp on the wheel–rail interaction force, for an inclination of 2 mrad and a speed of 140 km/h.

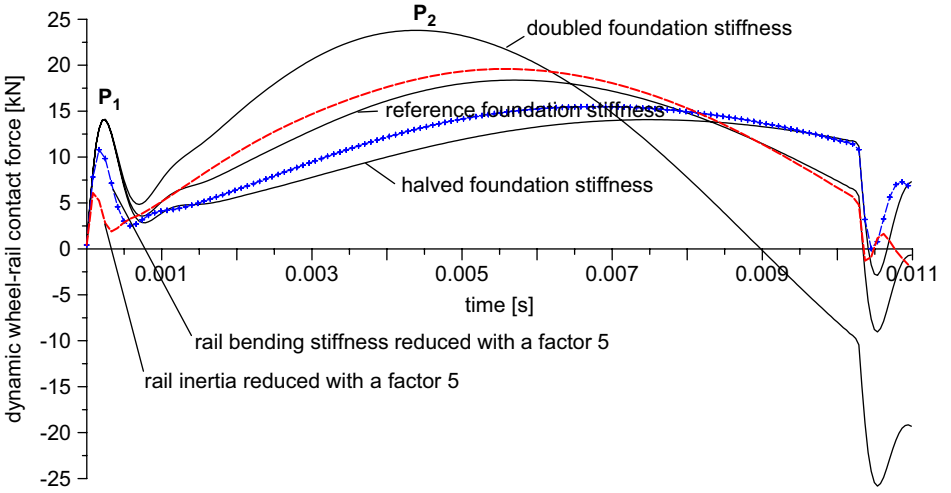

Fig. 7. Influence of the track parameters on the wheel–rail interaction force, for a ramp inclination of 2 mrad, a basis length of 400 mm and a train speed of 140 km/h.

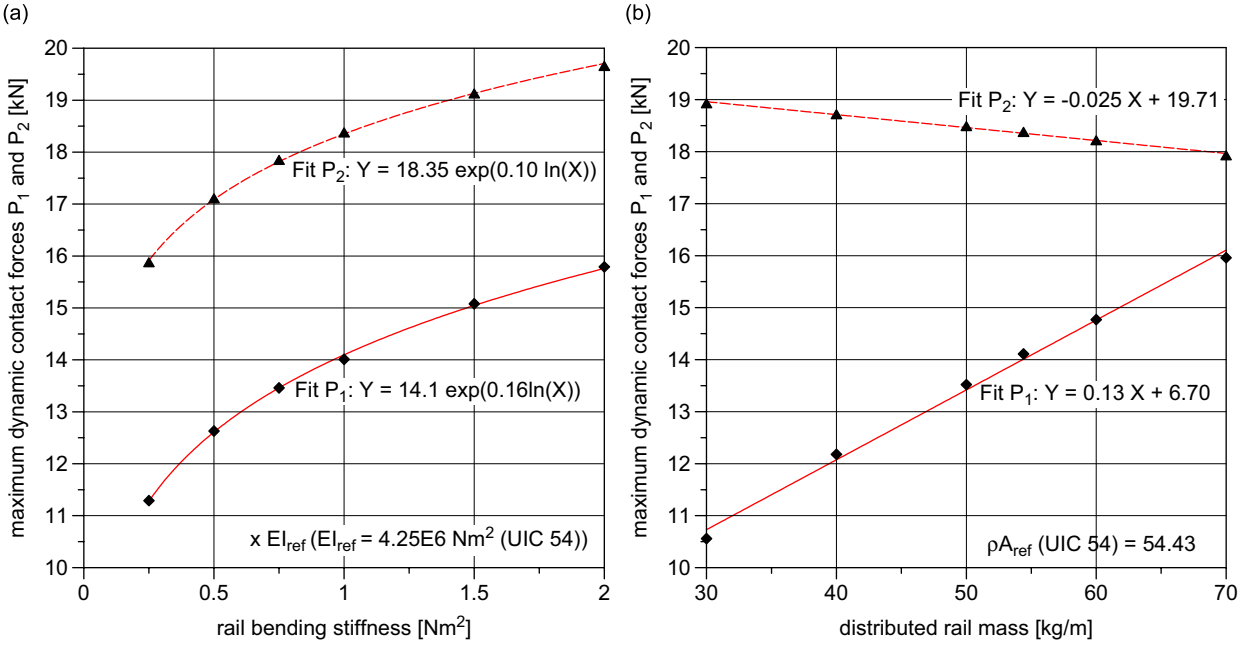

Fig. 8. Influence of the rail bending stiffness (a) and the rail mass (b) on the peak forces P_1 and P_2, for a ramp inclination of 2 mrad, a basis length of 400 mm and a train speed of 140 km/h.

The diagrams in Fig. 8 show the dependence of the P_1 and P_2 forces on the rail properties more into detail. As the linear influence of the slope θ and the velocity V is known, their values are taken constant, at 2 mrad and 38.9 m/s (140 km/h), respectively. In Fig. 8a, the influence of the rail bending stiffness (in comparison to the reference stiffness of 54 E1) on the magnitude of P_1 and P_2 is shown, for a constant rail mass (54 E1). In the region which is relevant for common rail profiles, both the trends for P_1 and P_2 show an approximating exponential behaviour as a function of the bending stiffness. In Fig. 8b, the influence of the distributed rail mass (for a constant bending stiffness (54 E1)) is shown. In the region of interest, the trends of both P_1 and P_2 can be approximated as linear. Both figures show that the influences of both the rail inertia and the rail bending stiffness on P_1 are most important, whereas the influence of the rail inertia on P_2 is negligible.

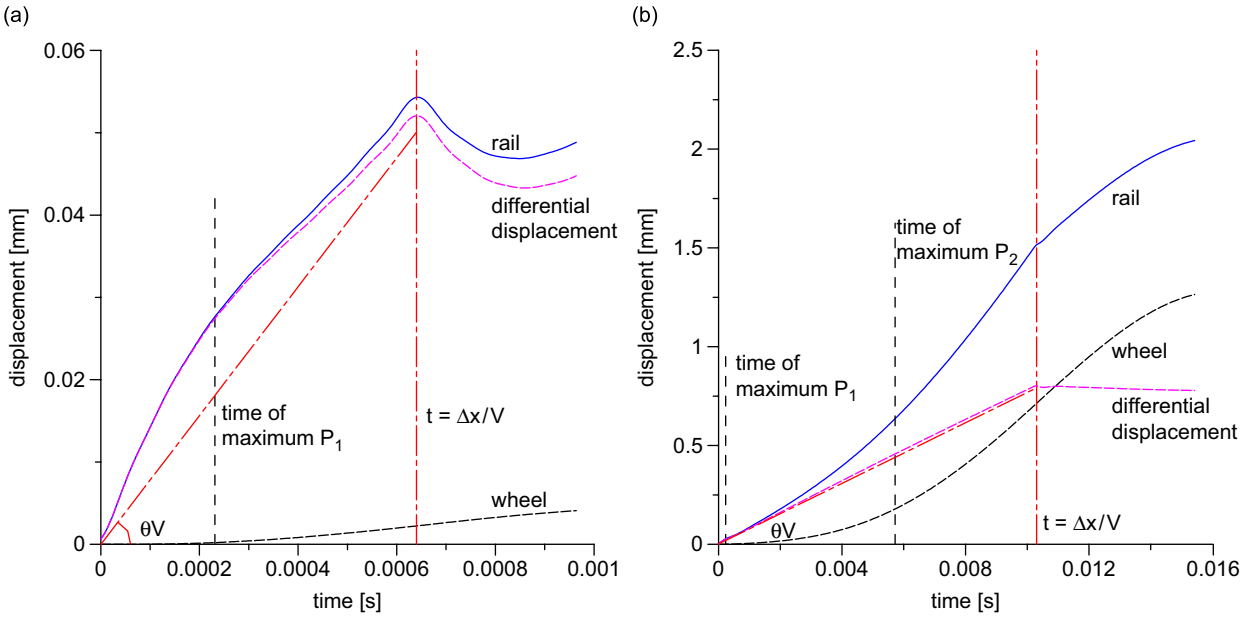

Fig. 9. Displacements of wheel and rail during the P_1 and P_2 wheel–rail interaction, for a ramp inclination of 2 mrad, a basis length of 25 (a) and 400 mm (b), respectively, and a train speed of 140 km/h.

It has been reported in Ref. [31] that during passage of a train wheel over a rail weld irregularity the track follows the excitation quasi-instantaneously, whereas the wheel displacement shows a delay in response relative to the track, owing to it larger inertia. This conclusion is verified with the present model in Fig. 9, where the displacements of the rail and the wheel are shown for a ramp of 2 mrad, a train velocity of 38.9 m/s (140 km/h) and a basis length of 25 mm (to study the P_1-behaviour; in Fig. 9a) and 400 mm (to study the P_2-behaviour; in Fig. 9b), respectively. In Fig. 9, also the differential displacement of the wheel and the rail is shown as a function of time. In the response of a mechanical system being dynamically excited, the elasticity and the inertia may dominate this response, dependant on the frequency content of the excitation. Comparison of the differential wheel and rail displacement to the excitation as a function of time gives an indication of the contribution of the elastic component to the dynamic interaction force relative to the inertial component. When the differential displacement and the excitation coincide, the response is quasi-static.

From Fig. 9a, in which also the excitation in the time domain is plotted, it can be concluded that the rail indeed follows the irregularity to a large extent during the P_1-interaction, whereas the wheel shows a negligible response within the considered time interval. The differential displacement, which almost coincides with the rail displacement, does not coincide with the excitation, revealing an important contribution of the inertial component to the P_1-force.

From the graph in Fig. 9b it can be concluded that the wheel and rail displacements both play an important role during the P_2-interaction. The differential displacement coincides almost exactly with the excitation, indicating a negligible contribution of the inertial component to the P_2-force.

In the previous section, the characteristics of the dynamic wheel–rail interaction at short-length rail irregularities without dominating wavelength have been studied with the basic ramp model. In the next section, the case of an arbitrary realistic geometry will be addressed. As has been mentioned in the Introduction, the focus is placed on rail welds.

7. Simulation results for measured welds

As has been explained in Ref. [30], the height of rail welds along the rail is measured electronically using digital straightedges with a finite sampling interval. The measurements used in this paper are based on the eddy current principle. The sampling interval equals 5 mm and the measurement basis is 1 m. The

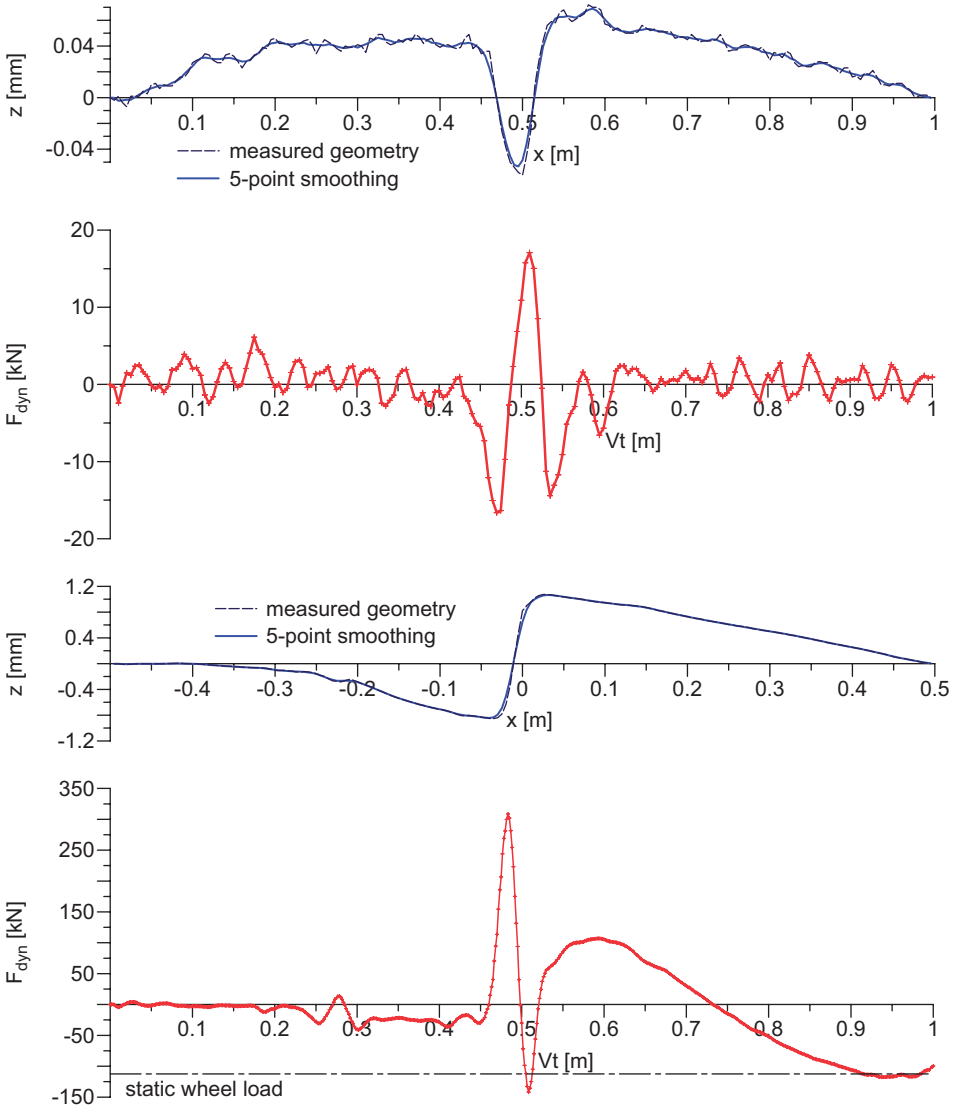

Fig. 10. Examples of measured welds (sampling interval 5 mm), geometry after 5-point smoothing and calculated time histories of the dynamic wheel–rail contact force at 140 km/h.

measurement signal cannot be used directly as an input in the simulations because the wheel–rail contact patch acts as a 'filter' for micro-asperities in the rail surface. The roughness on the 5 mm scale does not affect the dynamic wheel–rail interaction on the considered global scale, i.e. not accounting for the stress distribution within the contact patch. Therefore, a continuous 5-point-smoothing (running average over 25 mm) is applied to the measurement signal before using it as an input in the calculations. Other filters have been proposed in the literature, such as the well-known heuristic filter of Remington [41]. However the latter filter leads to negative values for short wavelengths just above the contact patch diameter. Here, a simple 5-point-smoothing (running average) of the discrete measurement data is chosen. In Ref. [42] it is shown that the effect of contact filters becomes only relevant for wavelengths comparable to or smaller than the size of the contact patch along the rail.

The graphs in Fig. 10 show examples of the time histories of the contact force according to expression (35) for two measured welds, for a train velocity of 38.9 m/s (140 km/h). Also shown are the measured geometry (sampling interval 5 mm) and the geometry after continuous 5-point-smoothing (i.e., the input for the

calculation). The first weld is rather well aligned, but it shows a high degree of roughness on a small scale (order 1 mm) and, at the centre, the effect of non-homogeneous shrinkage of the weld and parent material after the grinding process, which has obviously been performed at a too high temperature. The second weld is smooth on a micro-scale, but shows a severe misalignment before the rail ends have been welded together, resulting in a sharp step of about 2 mm in rail height over 25 mm. For the first weld the dynamic component of the contact force does not exceed 20 kN. For the second weld, the maximum dynamic force exceeds 300 kN, followed by a contact loss, since the dynamic force component exceeds the static preload (112.5 kN). The real maximum contact force is expected to be somewhat higher due to the nonlinear stiffening of the Hertzian contact spring during its almost instantaneous compression at $Vt = 0.47$ m. Furthermore, the linear calculation cannot deal with the contact loss. When the studied weld is overpassed in the track by trains in the positive x-direction, it will have a very short lifetime with a severe risk of brittle failure. At 83.3 m/s (300 km/h) the maximum force increases to more than 800 kN followed by a dip to less than -500 kN in a linear calculation, indicating repeated loss of contact and impact loading.

As has been stated before, a perfectly linear relation between $F_{\max}$ and $\theta_{\max}$ does not exist for an arbitrary irregularity due to the mutual influence of the force histories for each discrete slope, especially with the sampling interval approaching zero in a continuous signal. Therefore, the accuracy of any relationship between the extreme value of the contact force and a geometrical parameter of the irregularity depends on the statistical distribution of this geometrical parameter over the irregularity. For example, if the first derivative of the irregularity has a narrow distribution, the slope variation along the irregularity is restricted and the mutual influence of the time histories of the force for each discrete slope is also restricted.

In the previous section, the distribution of the discrete slopes was considered for a single given weld. Now, the distribution of the maximum absolute inclination for a large number of welds is considered. The higher this inclination, the more variation in slope is possible, implying that the mutual influence of the time histories of the contact force for the discrete slopes of a given irregularity will also increase. Therefore, when a large number of welds is considered, the scatter in the relationship between maximum inclinations and contact forces will increase with increasing maximum inclination, as will be confirmed by the results in the following.

In Ref. [31] a correlation analysis has been performed for a population of 239 measured rail welds, in which the relationships between different geometrical parameters of the welds and the variables describing the dynamic wheel–rail response were investigated with a FE model. The model developed in this paper is a practical tool to validate the results of this correlation analysis, for the same set of weld measurements. In order to keep this analysis concise, it will be restricted to the dynamic contact force, which is the most important variable.

In Fig. 11 the maximum absolute dynamic wheel–rail contact forces (during the time interval of overpassing the weld) are shown as a function of the maximum absolute inclinations of the welds. It is observed that the scatter in the forces increases with increasing maximum absolute inclination, as has been explained. For all velocities, a linear fit through the origin is shown; its equation and coefficient of determination are displayed too. Apart from the linear fits through the origin, also the linear regression lines are shown in the cases that the coefficients of determination R^2 for both cases differ. Similarly to the results obtained in Ref. [31], the correlation between forces and maximum inclinations increases significantly with the velocity. This can be explained by a more flat transfer of the system as the excitation frequency band shifts towards higher frequencies with increasing speed. For a perfectly flat transfer, there would be a perfect correlation between geometry and contact force.

For 38.9 m/s (140 km/h), the results are also shown on a logarithmic scale in Fig. 11; the results projected on both axes may then be represented as Gaussian distributed, with a given mean value. This result is valid for all velocities and will be addressed more extensively in Section 9.

In Fig. 11, the maximum absolute inclination of the 5-point-smoothed signal (with a sampling interval of 5 mm) is plotted on the horizontal axes. This signal, artificially 'filtered' by the contact patch, also served as an input in the force calculations; the timestep for the evaluation of the integrals was $\Delta t = 5\,\text{mm}/V$, which lead to convergent results. In the determination of the QI of rail welds [30,31], the maximum absolute inclination of this signal is taken on a different, 25 mm basis (only each 5th sampling point is used), resulting in a loss of information, but rendering the method more apt for practical purposes. Therefore, the results in Ref. [31] are not directly comparable to the results in Fig. 11. The relation between both the maximum absolute inclinations

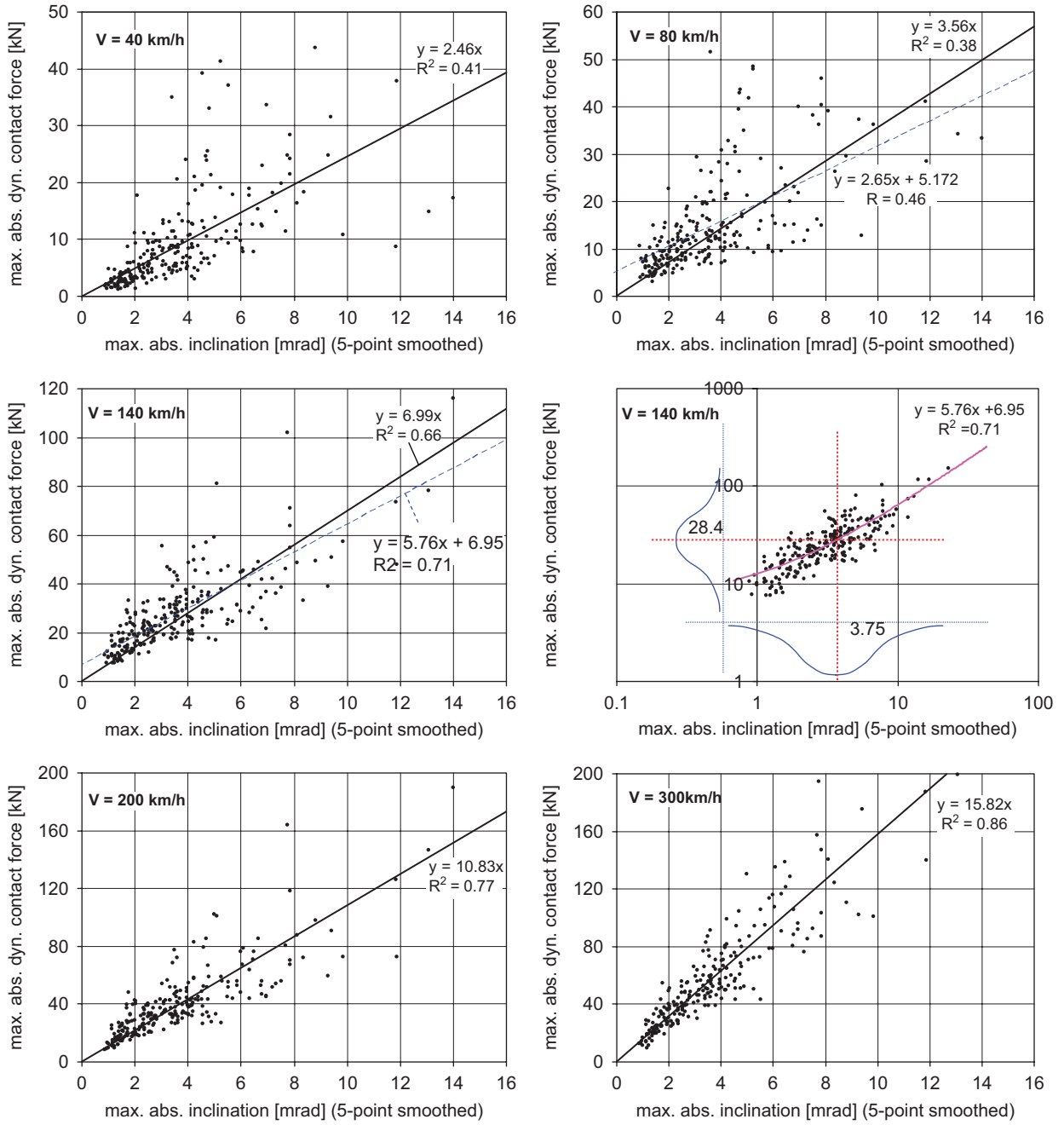

Fig. 11. Relationship between the maximum absolute inclination of the rail geometry and the maximum absolute value of the dynamic wheel–rail contact force for rail welds at different train speeds; for 140 km/h results are also shown on a log-scale with the corresponding Gaussian distributions and their mean values.

of the continuously 5-point-smoothed signal with the original sampling interval of 5 mm and the one with extended sampling interval of 25 mm (as used in the determination of the QI) is shown in Fig. 12. For correct comparison, it should be noted that the extension of the sampling basis results in a maximum absolute inclination which is equal to or smaller than the original inclination.

The linear relationships between the dynamic force and the maximum absolute inclination from Fig. 11 are reproduced in Fig. 13a for all train velocities. In Fig. 13b, the dependence of the dynamic force on the train

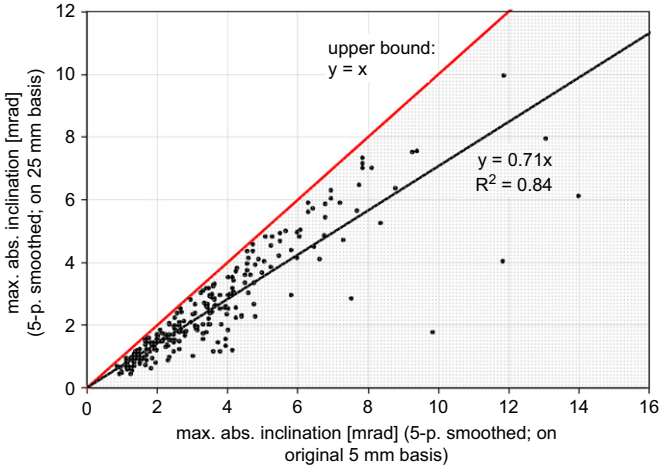

Fig. 12. Relationship between the maximum absolute inclinations of the continuously 5-point-smoothed signal with an extended sampling interval of 25 mm (used in the determination of the QI [2,3]) and of the 5-point-smoothed signal with the original sampling interval of 5 mm.

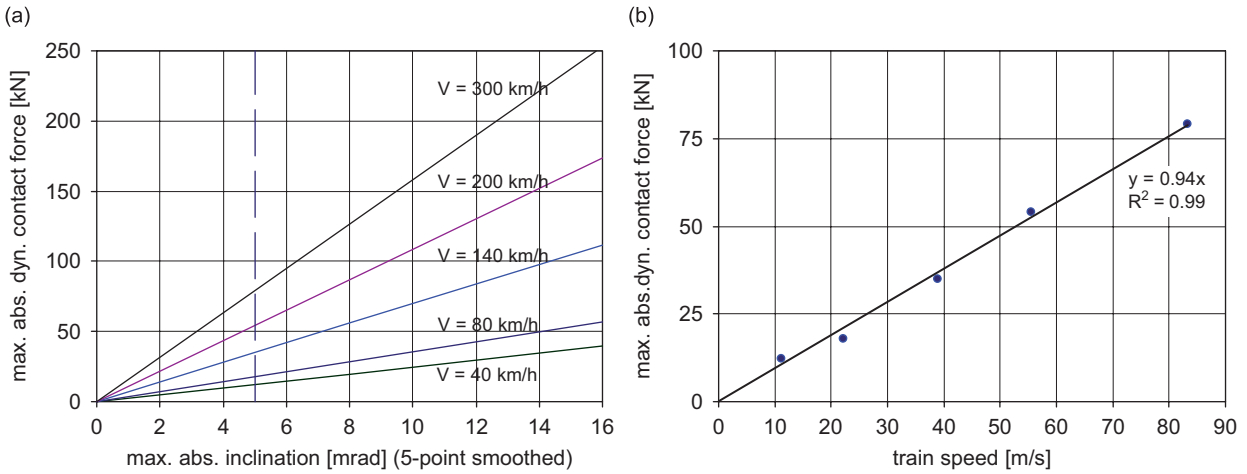

Fig. 13. Dependence of the dynamic wheel–rail contact force at welds on the maximum absolute inclination (for different train speeds) (a) and on the train speed (for a given maximum inclination of 5 mrad) (b).

speed is shown for a given maximum inclination (5 mrad). It is obvious that the relationship between the dynamic force and the train speed can be described very well as directly proportional, which confirms the results of the analysis performed in Ref. [31].

With the results shown in Fig. 13, the coefficient γ in the general relationship (38) can be validated for rail welds, resulting into the following normalised expression:

$$\frac{F_{\mathrm{dyn,max}}}{F_{\mathrm{ref}}} = 0.19\,\theta\,\frac{V}{V_{\mathrm{ref}}} \quad (F\,(\mathrm{kN}),\quad V\,(\mathrm{m/s}),\quad \theta\,(\mathrm{mrad}),\quad F_{\mathrm{ref}} = 1\,\mathrm{kN},\quad V_{\mathrm{ref}} = 1\,\mathrm{m/s}). \tag{41}$$

From the analysis in Ref. [31], $\gamma = 0.22$ was found for rail welds. In this paper, $\gamma = 0.18$ was found for the perfectly linear relationship for the theoretical case of a ramp with one single slope, and $\gamma = 0.19$ for rail welds. The numbers are very close; the somewhat higher value from Ref. [31] may be explained from the fact that inclinations on a 25 mm basis have been used. As has been remarked before (Fig. 12), the inclination can only decrease when the sample interval is extended from 5 to 25 mm. Because the forces remain unaffected, the

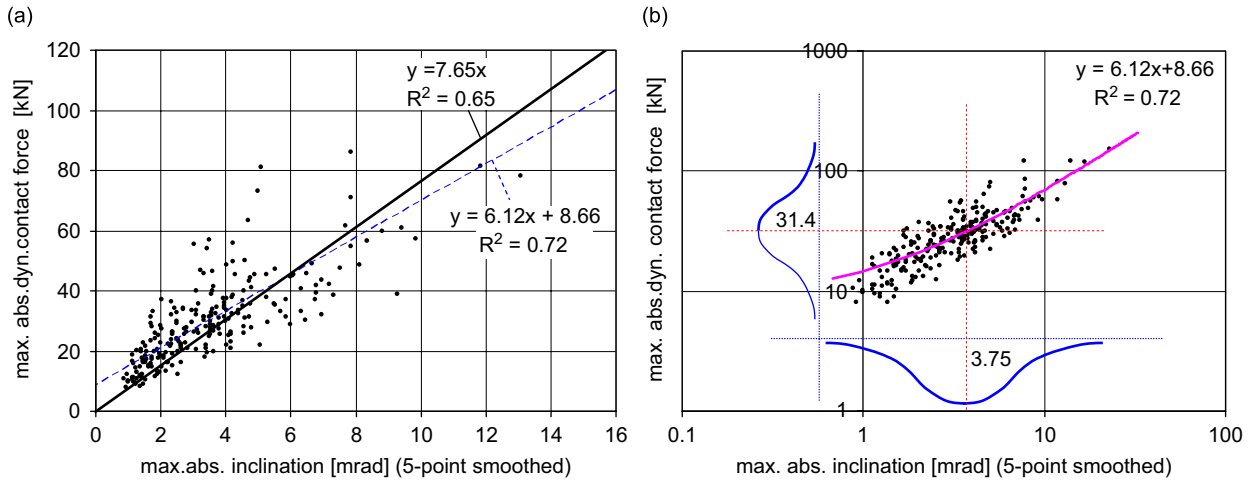

Fig. 14. Relationship between the maximum absolute inclination of the rail geometry and the maximum absolute value of the dynamic wheel–rail contact force for rail welds at 140 km/h; the welds are passed in both directions (results on linear (a) and logarithmic (b) scales).

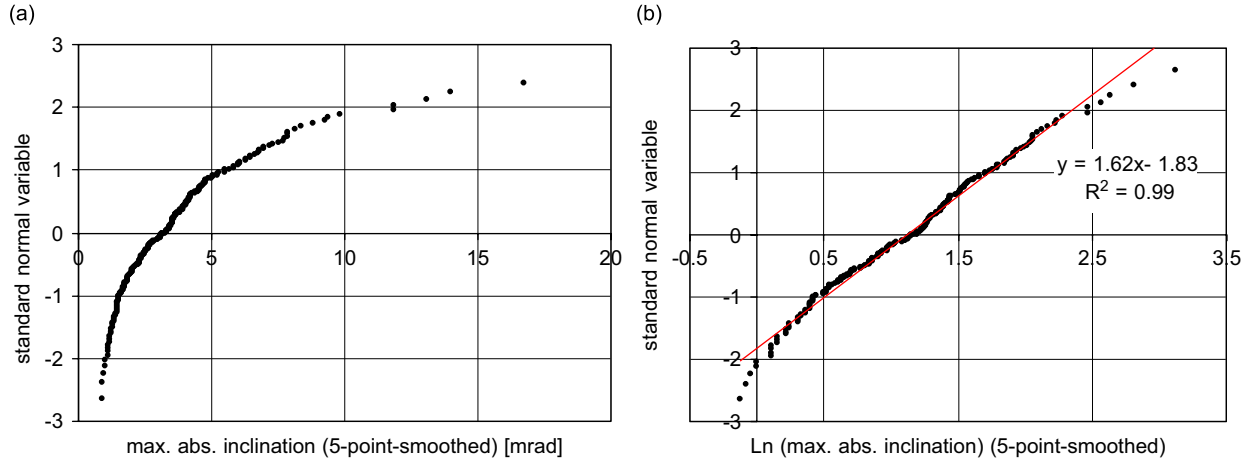

Fig. 15. Maximum absolute inclinations of the weld geometry as a function of the standard normal variable; normal probability test (a) and lognormal probability test (b).

coefficient will then increase. Further, the difference in the models applied in this paper and in Ref. [31] is not expected to affect the results significantly. It can be concluded that $\gamma \approx 0.2$ in practice (for 54 E1 rail).

Gullers et al. [43, Figs. 8 and 9] show examples of measured wheel–rail contact forces on the Swedish network (7 peaks in about 22 m); also the geometry of an irregularity corresponding to one of the peaks (without indication to the exact position of the peak) is given. Application of formula (41) yields for this case ($\theta \approx 15$ mrad; $V = 48.6$ m/s): $F_{\mathrm{dyn,max}} = 0.19 \times 15 \times 48.6 = 139$ kN. The static load of 60 kN yields a total maximum load of 199 kN. The order of magnitude (ranging from 150 to 200 kN for all force peaks) is correct.

The results in Fig. 11 are for a train, passing the welds in one single direction. This is realistic for a railway network, on which trains, on a given piece of track, commonly run in only one direction. However, the development of the force is dependant on the train running direction. Therefore, one would expect a better correlation between maximum absolute inclinations (which are direction-independent) and forces if the extreme value of the force is taken for a train passing the welds in both directions. The results are shown for 38.9 m/s (140 km/h) in Fig. 14. It is observed that the gradient of the linear fit increases (indicating a higher force level for a given maximum absolute inclination), whereas the correlation does not change significantly.

This is confirmed by the results for the other velocities; the force levels when considering two directions are about 5–10% higher than in the case of only one running direction.

8. Statistical properties of wheel–rail interaction at rail welds

In Ref. [30] it has been demonstrated that the discrete first derivatives of rail welds are Gaussian distributed with zero mean value (except for the tails). The maximum discrete first derivatives of a large population of welds proved to be very well approximated by a lognormal distribution.

In Fig. 15, the maximum absolute inclination and its logarithm (for the 5-point-smoothed signals) are shown as a function of the standard normal variable for the measured weld sample which was used in the simulations. If the logarithm is taken, the result is approximately linear. This confirms that the maximum absolute inclination of a large number of rail welds may be represented by a lognormal distribution. Therefore, the projections of the data points in Figs. 11 and 14 on the horizontal axes may be considered as lognormally distributed (as is shown in Figs. 11 and 14 for 38.9 m/s (140 km/h)).

Now, the distribution of the maximum dynamic forces in Fig. 11, for the whole sample, is addressed. Thus, the projection of the data points on the vertical axes is considered. This distribution gives the distribution of the dynamic forces occurring over a railway network at welds, for a given distribution of the maximum absolute inclinations of the welds. It gives no information about the scatter in the deterministic relationship

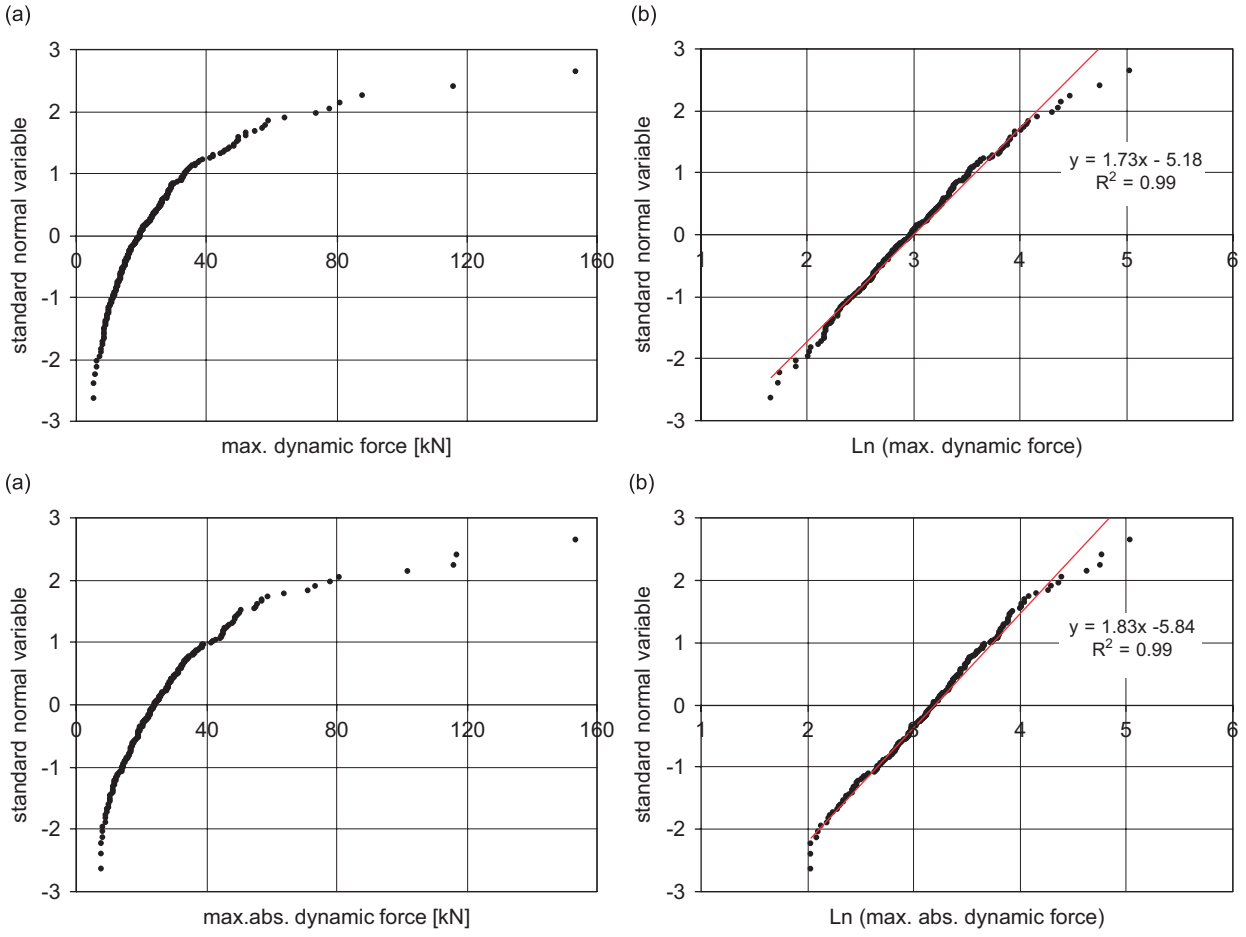

Fig. 16. Maximum dynamic contact forces and maximum absolute dynamic forces (for 140 km/h) as a function of the standard normal variable; normal probability test (a) and lognormal probability test (b).

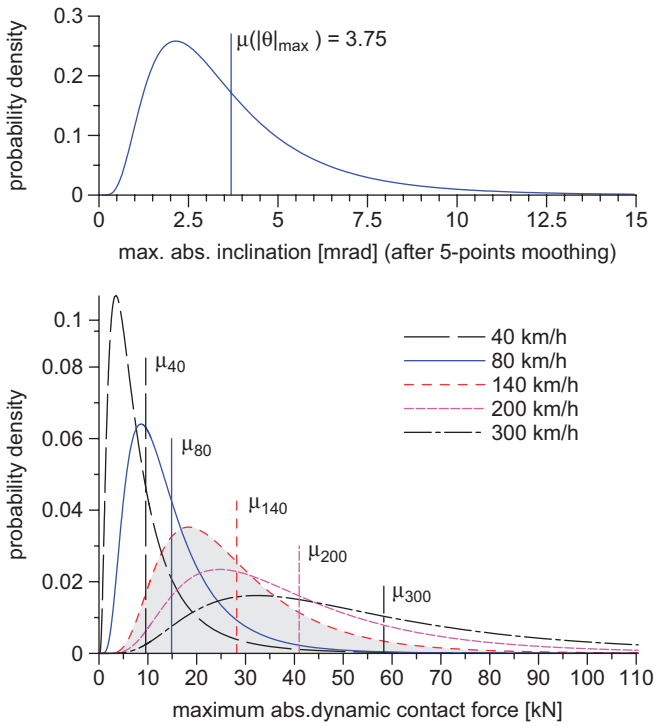

Fig. 17. Lognormal distribution of the maximum absolute inclination of rail welds and corresponding lognormal distributions of the maximum absolute values of the dynamic wheel–rail contact force at different train velocities.

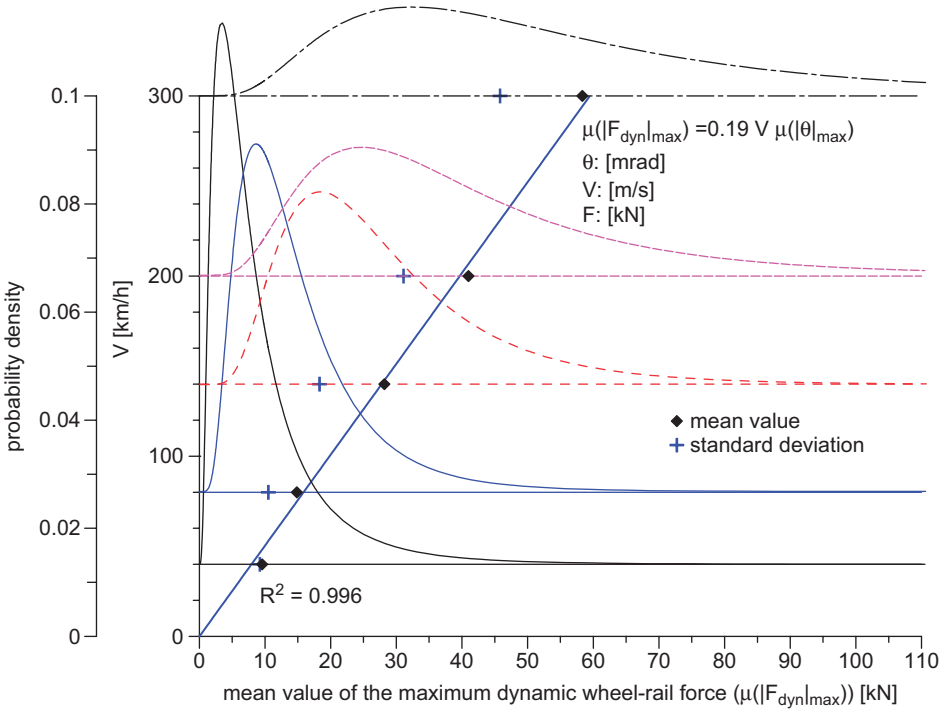

Fig. 18. Linear relationship between the mean value of the extreme dynamic wheel–rail contact forces and the train velocity for a weld population with a given mean value for the maximum inclination. The contact force distributions are shown as a function of the train speed.

Table 2
Statistical properties of rail weld geometry (239 measurements) and maximum dynamic contact forces

	Mean value	Standard deviation	Coefficient of variation
Maximum absolute inclination	3.75 mrad	2.7 mrad	0.72
Force: 40 km/h	9.6 kN	9.2 kN	0.96
Force: 80 km/h	15.0 kN	10.5 kN	0.70
Force: 140 km/h	28.4 kN	18.3 kN	0.64
Force: 200 km/h	41.5 kN	31.1 kN	0.75
Force: 300 km/h	58.8 kN	45.8 kN	0.78

(41), for a given inclination; this aspect, which is linked to a vertical cross-section in Fig. 11, will be addressed later.

In Fig. 16a, the maximum dynamic contact forces and the maximum of their absolute values are plotted as versus the standard normal variable ($V = 38.9$ m/s (140 km/h)). In Fig. 16b, this is repeated for the logarithm of the forces. The resulting functions in Fig. 16b can be well approximated by a straight line (a base of 10 leads to similar results). This result is valid for all velocities. Therefore, the maximum dynamic contact force occurring at rail welds may be represented by a lognormal distribution, with mean and standard deviation varying as a function of the train speed. In Fig. 11 this is shown for 38.9 m/s (140 km/h) (vertical axis).

In Fig. 17 the probability density functions of the maximum absolute inclination and of the maximum dynamic contact force are shown for different velocities. The probability density function of the force shifts towards higher values with increasing speed, the top value drops and the function becomes more 'stretched'.

Fig. 18 shows the linear relationship between the mean value of the maximum dynamic wheel–rail contact force and the train velocity. For different velocities, the probability density corresponding to the force distributions is now quantified on a separate vertical axis. The values of the statistical parameters of the distributions are given in Table 2. With Fig. 15 the distribution of forces occurring at rail welds over a railway network can be easily estimated for different train velocities, once the mean value of the maximum absolute inclination of a population of measured rail welds is known. The standard deviation must be estimated as a percentage of the mean value. For this reason also the coefficient of variation is given in Table 2, as a measure of the statistical dispersion of the force. There is no clear link between the standard deviation and the velocity, which is related to the non-uniform frequency transfer of the wheel–rail system.

The graphs in Figs. 11 and 14 show a considerable scatter in the results for a given inclination. Studying the results for a given inclination is equivalent to considering a vertical cross-section in the graphs. This scatter in the deterministic relationship (41) is due to the impossibility to reduce the dynamic wheel–rail interaction to a purely geometrical problem. The fact that the scatter in the results increases with increasing inclination was already explained in the previous section. However, the distribution of the forces for a given inclination and its relation to the value of the inclination cannot be further analysed, by lack of data: 4 values of the inclination with 5 data points (4 sets of 5 welds with the same maximum absolute inclination) and 1 inclination value with 6 data points are available; all other inclination values occur less frequently. Therefore, results of the normal or lognormal probability test do not give a clear answer.

9. Discussion and conclusions

In Section 7, the time-scale of the P_1 peak was found to range from about 0.5 to 0.75 ms, which corresponds to a length-scale (half-wavelength) of about 20–30 mm at a regular line-speed of 38.9 m/s (140 km/h). At 69.4 m/s (250 km/h; high-speed lines) the length-scale corresponding to the P_1 force is about 35–48 mm (the time-scale does not vary significantly). Short-pitch rail corrugations have a wavelength which typically ranges from 25 to 80 mm. This means that non-smooth irregularities causing P_1 forces can be an important source of short-pitch corrugations.

Based on laboratory experiments, in Ref. [44] a corrugation mechanism was proposed, initiated by excitation of a 'contact resonance' in the wheel–rail interface, as can be easily excited at a weld. The resonance

Fig. 19. Squats in the hardness minima in the heat-affected zone at the surface of an aluminothermic rail weld.

in the interface leads to periodically varying micro-slip and wear in the contact, causing short-pitch corrugations. However, the wavelength of such corrugations should be proportional to the speed, which is not or only very weakly observed in practice.

Not all aspects of the corrugation process can be explained by a fluctuating contact load or fixed resonances or anti-resonances of the wheel–track system, as pointed out in Refs. [45,46]. However, since the contact mechanics in the plane of the wheel–rail interface are directly related to the contact mechanics in the normal plane, a non-constant contact force must have a significant impact on the formation of corrugations [17,47–49]. Rail welds, which moreover exhibit non-constant metallurgical properties along the rail surface, therefore are often considered, and also observed in practice, as possible corrugation or also squat initiators, as observed in Refs. [16,19,20] (see Fig. 19). The studies in Refs. [21,32] showed the importance of the smoothness of the rail surface and the level of dynamic contact forces also for the initiation or propagation of RCF. The effect of a fluctuating contact load on non-uniform plastic deformation (shakedown) along an irregular rail was investigated in Ref. [50].

In this paper, a model for dynamic wheel–rail interaction at rail irregularities of arbitrary geometry has been developed. The model was formulated in the frequency domain, leading to relatively simple closed-form solutions for the variables describing the dynamic wheel–rail interaction.

This model has been applied to investigate the basic features of dynamic wheel–rail interaction for short rail irregularities with a broad-band spectrum. For the theoretical case of a ramp in the longitudinal rail surface, the maximum contact force (P_1) has been proven to be directly proportional to the inclination of the ramp and the train speed. The influence of the rail properties (bending stiffness and distributed mass) on the contact force has been investigated. The results showed that (i) P_1 and P_2 increase with increasing bending stiffness, (ii) P_1 increases strongly and approximately linearly with increasing rail mass, and (iii) that P_2 decreases slightly with increasing rail mass. During P_1-interaction, the rail follows a surface irregularity to a large extent, whereas the wheel displacement is negligible. Both inertial and elastic contributions to the dynamic force are of major importance within this time interval. During P_2-interaction both wheel and rail displacements have comparable magnitudes. The inertial component of the dynamic force is negligible in comparison to the elastic one.

Furthermore, the model has been applied to calculate dynamic wheel–rail contact forces for a sample population of measured rail welds. Relationships between the maximum dynamic contact force, the maximum absolute inclination of a weld and the train speed have been derived. Finally, the statistical distribution of dynamic forces at welds occurring over a railway network has been considered, given a scan of the weld quality. These distributions proved to be lognormal. The distribution functions have been derived as a function of the average running speed and the mean value and standard deviation of the lognormally distributed maximum absolute weld inclinations.

Acknowledgements

The presented research is part of a research programme on the relationship between track geometry in the short-wave regime, dynamic train–track interaction and track deterioration, funded by the Dutch Railway Administrator ProRail (programme of Rolf Dollevoet). ProRail is also acknowledged for the availability of measurement data. The presented research will make part of a Ph.D. under the supervision of emeritus Prof. Coenraad Esveld.

References

[1] M.J.M.M. Steenbergen, Modelling of wheels and rail discontinuities in dynamic wheel–rail contact analysis, *Vehicle System Dynamics* 44 (2006) 763–787.
[2] E. Kabo, J.C.O. Nielsen, A. Ekberg, Prediction of dynamic train–track interaction and subsequent material deterioration in the presence of insulated rail joints, *Vehicle System Dynamics* 44 (2006) 718–729.
[3] W. Cai, Z. Wen, X. Jin, W. Zhai, Dynamic stress analysis of rail joint with height difference defect using finite element method, *Engineering Failure Analysis* 14 (2007) 1488–1499.
[4] A. Skyttebol, Continuous Welded Railway Rails: Residual Stress Analyses, Fatigue Assessments and Experiments, PhD Thesis, Chalmers University of Technology, 2004.
[5] Y. Terashita, M. Tatsumi, Analysis of damaged rail weld, *Quarterly Report of Railway Technical Research Institute* 44 (2003) 59–64.
[6] H. Shitara, Y. Terashita, M. Tatsumi, Y. Fukada, Nondestructive testing and evaluation methods for rail welds in Japan, *Quarterly Report of Railway Technical Research Institute* 44 (2003) 53–58.
[7] Y. Chen, F.V. Lawrence, C.P.L. Barkan, J.A. Dantzig, Heat transfer modelling of rail thermite welding, *Proceedings of the Institution of Mechanical Engineers, Part F: Journal of Rail and Rapid Transit* 220 (2006) 207–217.
[8] Y. Chen, F.V. Lawrence, C.P.L. Barkan, J.A. Dantzig, Weld defect formation in rail thermite welds, *Proceedings of the Institution of Mechanical Engineers, Part F: Journal of Rail and Rapid Transit* 220 (2006) 373–384.
[9] N. Ilic, M.T. Jovanovic, M. Todorovic, M. Trtanj, P. Saponjic, Microstructural and mechanical characterization of postweld heat-treated thermite weld in rails, *Materials Characterisation* 43 (1999) 243–250.
[10] P.J. Webster, G. Mills, X.D. Wang, W.P. Kang, T.M. Holden, Residual stresses in alumino-thermic welded rails, *Proceedings of the Institution of Mechanical Engineers, Journal of Strain Analysis* 32 (1997) 389–400.
[11] D. Tawfik, O. Kirstein, P.J. Mutton, W.K. Chiu, Verification of residual stresses in flash-butt-weld rails using neutron diffraction, *Physica B* 385–386 (2006) 894–896.
[12] D. Tawfik, P.J. Mutton, W.K. Chiu, Experimental and numerical investigations: alleviating tensile residual stresses in flash-butt welds by localised rapid post-weld heat treatment, *Journal of Materials Processing Technology* (2007).
[13] A. Skyttebol, B.L. Josefson, J.W. Ringsberg, Fatigue crack growth in a welded rail under the influence of residual stresses, *Engineering Fracture Mechanics* 72 (2005) 271–285.
[14] M. Ishida, T. Moto, A. Kono, Y. Jin, Influence of loose sleeper on track dynamics and bending fatigue of rail welds, *Quarterly Report of Railway Technical Research Institute* 40 (1999) 80–85.
[15] P.J. Mutton, E.F. Alvarez, Failure modes in aluminothermic rail welds under high axle load conditions, *Engineering Failure Analysis* 11 (2004) 151–166.
[16] M. Hiensch, J.C.O. Nielsen, E. Verheijen, Rail corrugation in the Netherlands—measurements and simulations, *Wear* 253 (2002) 140–149.
[17] J.C.O. Nielsen, R. Lundén, A. Johansson, T. Vernersson, Train–track interaction and mechanisms of irregular wear on wheel and rail surfaces, *Vehicle System Dynamics* 40 (2003) 3–54.
[18] A. Ekberg, E. Kabo, J.C.O. Nielsen, R. Lunden, Subsurface initiated rolling contact fatigue of railway wheels as generated by rail corrugation, *International Journal of Solids and Structures* (2007).
[19] Z. Li, X. Zhao, C. Esveld, R. Dollevoet, Causes of squats: correlation analysis and numerical modeling, *Proceedings of the Seventh International Conference on Contact Mechanics and Wear of Rail/Wheel Systems CM 2006*, Brisbane, Australia, 2006.
[20] Z. Li, X. Zhao, C. Esveld, R. Dollevoet, Rail stresses, strain and fatigue under dynamic wheel–rail interaction, *Proceedings of the International Heavy Haul Conference IHHA 2007*, Kiruna, Sweden, 2007.
[21] E. Kabo, Material defects in rolling contact fatigue—influence of overloads and defect clusters, *International Journal of Fatigue* 24 (2002) 887–894.
[22] K. Dang Van, M.H. Maitournam, Rolling contact in railways: modelling, simulation and damage prediction, *Fatigue and Fracture of Engineering Materials and Structures* 26 (2003) 939–948.
[23] F.J. Franklin, T. Chung, A. Kapoor, Ratcheting and fatigue-led wear in rail–wheel contact, *Fatigue and Fracture of Engineering Materials and Structures* 26 (2003) 949–955.
[24] D.I. Fletcher, F.J. Franklin, A. Kapoor, Image analysis to reveal crack development using a computer simulation of wear and rolling contact fatigue, *Fatigue and Fracture of Engineering Materials and Structures* 26 (2003) 957–967.
[25] J.R. Evans, M.C. Burstow, Vehicle/track interaction and rolling contact fatigue in rails in the UK, *Vehicle System Dynamics* 44 (2006) 708–717.

[26] S.L. Srimani, A.C. Pankaj, J. Basu, Analysis of end straightness of rail during manufacturing, *International Journal of Mechanical Sciences* 47 (2005) 1874–1884.
[27] D.F. Cannon, K.O. Edel, S.L. Grassie, K. Sawley, Rail defects: an overview, *Fatigue and Fracture of Engineering Materials and Structures* 26 (2003) 865–887.
[28] A. Caprioli, A. Cigada, D. Raveglia, Rail inspection in track maintenance: a benchmark between the wavelet approach and the more conventional Fourier analysis, *Mechanical Systems and Signal Processing* 21 (2007) 631–652.
[29] M. Bocciolone, A. Caprioli, A. Cigada, A. Collina, A measurement system for quick rail inspection and effective track maintenance strategy, *Mechanical Systems and Signal Processing* 21 (2007) 1242–1254.
[30] M.J.M.M. Steenbergen, C. Esveld, Rail weld geometry and assessment concepts, *Proceedings of the Institution of Mechanical Engineers, Part F: Journal of Rail and Rapid Transit* 220 (2006) 257–271.
[31] M.J.M.M. Steenbergen, C. Esveld, The relation between the geometry of rail welds and the dynamic wheel–rail response; numerical simulations for measured welds, *Proceedings of the Institution of Mechanical Engineers, Part F: Journal of Rail and Rapid Transit* 220 (2006) 409–424.
[32] J.C.O. Nielsen, A. Ekberg, R. Lundén, Influence of short-pitch wheel/rail corrugation on rolling contact fatigue of railway wheels, *Proceedings of the Institution of Mechanical Engineers, Part F: Journal of Rail and Rapid Transit* 219 (2006) 177–187.
[33] J.C.O. Nielsen, High-frequency vertical wheel–rail contact forces—validation of a prediction model by field testing, *Proceedings of the Seventh International Conference on Contact Mechanics and Wear of Rail/Wheel Systems CM 2006*, Brisbane, Australia, 2006.
[34] E.G. Berggren, M.X.D. Li, J. Spännar, A new approach to the analysis and presentation of vertical track geometry quality and rail roughness with focus on track–track interaction and wavelength content, *Proceedings of the Seventh International Conference on Contact Mechanics and Wear of Rail/Wheel Systems CM 2006*, Brisbane, Australia, 2006.
[35] T.X. Wu, D.J. Thompson, Theoretical investigation of wheel–rail non-linear interaction due to roughness excitation, *Vehicle System Dynamics* 34 (2000) 261–282.
[36] T.D. Armstrong, D.J. Thompson, Use of a reduced scale model for the study of wheel/rail interaction, *Proceedings of the Institution of Mechanical Engineers, Part F: Journal of Rail and Rapid Transit* 220 (2006) 235–246.
[37] T. Mazilu, Green's functions for analysis of dynamic response of wheel/rail to vertical excitation, *Journal of Sound and Vibration* 306 (2007) 31–58.
[38] S.L. Grassie, R.W. Gregory, D. Harrison, K.L. Johnson, The dynamic response of railway track to high-frequency vertical excitation, *Journal of Mechanical Engineering Science* 24 (1982) 77–90.
[39] C. Esveld, *Modern Railway Track*, second ed., MRT-productions, Zaltbommel, The Netherlands, 2001.
[40] A.P. de Man, Dynatrack—A Survey of Dynamic Railway Properties and their Quality, PhD Thesis, Delft University of Technology, 2002.
[41] P.J. Remington, Wheel–rail noise, parts I–IV, *Journal of Sound and Vibration* 46 (1976) 359–451.
[42] R.A.J. Ford, D.J. Thompson, Simplified contact filters in wheel/rail noise prediction, *Journal of Sound and Vibration* 293 (2006) 807–818.
[43] P. Gullers, L. Andersson, R. Lundén, High-frequency vertical wheel–rail contact forces—field measurements and influence of track irregularities, *Proceedings of the Seventh International Conference on Contact Mechanics and Wear of Rail/Wheel Systems CM 2006*, Brisbane, Australia, 2006.
[44] S.L. Grassie, K.L. Johnson, Periodic microslip between a rolling wheel and a corrugated rail, *Wear* 101 (1985) 291–309.
[45] T.X. Wu, D.J. Thompson, An investigation into rail corrugation due to micro-slip under multiple wheel–rail interactions, *Wear* 258 (2005) 1115–1125.
[46] S. Müller, A linear wheel–track model to predict instability and short pitch corrugation, *Journal of Sound and Vibration* 227 (1999) 899–913.
[47] A. Igeland, H. Ilias, Rail head corrugation growth predictions based on non-linear high frequency vehicle–track interaction, *Wear* 213 (1997) 90–97.
[48] K. Hempelmann, F. Hiss, K. Knothe, B. Ripke, The formation of wear patterns on rail tread, *Wear* 144 (1991) 179–195.
[49] K. Hempelmann, K. Knothe, An extended linear model for the prediction of short pitch corrugation, *Wear* 191 (1996) 161–169.
[50] A. Böhmer, T. Klimpel, Plastic deformation of corrugated rails—a numerical approach using material data of rail steel, *Wear* 253 (2002) 150–161.